Single-atoms Ru/NiFe layered double hydroxide electrocatalyst: Efficient for oxidation of selective oxidation of 5-hydroxymethylfurfural and oxygen evolution reaction

Haocheng Xu [a,b], Guorong Xin [a,b], Wenxuan Hu [a,b], Zhengxiong Zhang [a,b], Chuanling Si [c], Jingguang Chen [a,b], Lefu Lu [a,b], Yutao Peng [a,b], Xiaoyun Li [a,b,*]

[a] School of Agriculture, Shenzhen Campus of Sun Yat-sen University, Shenzhen, Guangdong 518107, China
[b] School of Agriculture, Sun Yat-sen University, Guangzhou, Guangdong 510275, China
[c] Tianjin Key Laboratory of Pulp and Paper, Tianjin University of Science and Technology, Tianjin 300457, China

ARTICLE INFO

ABSTRACT

The adsorption performance modulation of catalysts on reactants is effective for the improvement of catalytic oxidation reactions. Ru is beneficial for adsorption of products. Here, the single Ru atoms were supported on NiFe layered double hydroxide (LDH) ($Ru_{0.3}$/NiFe) to enhance the adsorption capacity of catalyst using a two-step electrodeposition method. $Ru_{0.3}$/NiFe was used in the oxygen evolution reaction (OER) and the selective oxidation of 5-hydroxymethylfurfural (HMFOR). $Ru_{0.3}$/NiFe showed extremely low overpotential (243 mV at 10 mA cm^{-2}) and excellent durability in OER. $Ru_{0.3}$/NiFe exhibits excellent HMF conversion (99.43%), 2,5-furan dicarboxylic acid (FDCA) selectivity (99.24%) and yield (98.68%) in HMFOR. The possible HMFOR reaction pathway was further studied, revealing that the load of Ru enhances the path from HMF to DFF, thereby improving the yield of FDCA. Both the outcomes of experimental findings and density functional theory (DFT) calculations indicate that increasing the composition of Ru optimizes the adsorption energy of HMF compared to NiFe, allowing FeNiOOH to more efficiently capture protons and electrons in HMFOR.

1. Introduction

The overconsumption of fossil fuels has resulted in a multitude of environmental problems, including white pollution, air pollution, and the significant emission of carbon dioxide. To combat this issue, renewable green biomass and biomass-derived platform chemicals offer a promising avenue for the synthesis of value-added chemicals and biofuels as a replacement for fossil fuels [1,2]. HMF (5-hydroxymethylfurfural), a furan compound, can be converted into a variety of high-value chemical compounds to replace fossil fuels [3]. Among a series of high-value chemicals converted by HMF, 2,5-furan dicarboxylic acid (FDCA) is an important intermediate of numerous high-value chemicals and furan-based polymers [4].

The traditional preparation method of FDCA is catalytic oxidation of HMF at high temperature with O_2, which requires excessive amounts of oxidant, high energy consumption and complex reaction equipment [3,5]. Therefore, it is necessary to develop a catalytic system for efficient conversion of HMF to FDCA at normal temperature and pressure.

Electrocatalysis, as a novel catalytic method, has several advantages over thermal catalysis, including: (i) operating under mild reaction conditions; (ii) faster reaction rates and shorter reaction times; (iii) ease of control; and (iv) simpler reaction devices[6,7]. Furthermore, opting for the biomass platform chemical HMF with a lower standard electrode potential as the anode reaction in contrast to the typical oxygen evolution reaction (OER) not only enhances the energy conversion efficiency, but also generates products of greater value [8–11].

NiFe layered double hydroxides (LDH) catalysts have widely been studied for electrocatalytic the selective oxidation of 5-hydroxymethylfurfural (HMFOR) and OER [7,12]. The HMF conversion and FDCA selectivity of NiFe LDH can reach more than 80% under basic and base-free conditions[7,13]. For OER reaction, $Ni_{0.3}Fe_{0.7}$-LDH@NF showed an ultra-low over-potential of less than 200 mV at 10 mA cm^{-2} [14] The catalytic mechanism of NiFe in OER has been reported in a large number of literatures [15–17]. The iron cation in NiFe hydrotalcite is the active site in OER, which has been proven based on both experimental and calculated results [15,18]. Additionally, the high-valent

---

nickel ions are also active sites mentioned by other studies [19–21]. While reaching a general consensus can be difficult, there are some typically detailed explanations for its catalytic mechanism. However, what is the catalytic efficiency of NiFe-LDH in the oxidation process of the biomass platform compound HMF?

The catalytic activity of the above NiFe-LDH catalyst is limited by the proportional relationship of NiFe [22]. Based on experimental and computational results, the catalytic behavior of NiFe-LDH is classified as a single adsorption and scaling relationship [20,22,23]. However, for complex reactions involving multiple intermediates (such as OER and HMFOR), the single site of NiFe usually follows a linear proportional relationship, and the bond with one or more intermediates is too strong or too weak [24]. The catalyst surface introduces additional and more accessible active sites and optimizes the electronic structure, which could break the ratio limit and improve the catalytic capability. Among others, in the OER process, the Ta-modified orbit induced through charge transfer is favorable for the adsorption of -OH by the additional Ta sites in NiFe-LDH [25].

The introduction of single atoms on the surface of NiFe-LDH can not only maximize the utilization efficiency of atoms, but also obtain a large number of active sites [26,27]. Researchers found that the local electronic configuration and the induction of quantum size effect can be modified by adjusting the atomic coordination number [28–30]. Electronic metal-support interactions (EMSIs) have the capability to modify the electronic structure of the catalyst in a way that enhances the adsorption energy of intermediate species [31–33]. Among them, noble metal single-atom catalysts (NMSAC) have higher intrinsic activity and durability[34]. The low cost of Ru, and the appropriate binding strength between Ru and intermediates make single Ru atoms catalysts stand out [35–38]. Sun et al. found that the introduction of single Ru atoms can modulate the electronic structure of the support, thus optimizing the binding strength of H* and H_2O [39]. Furthermore, due to the interaction between Ru and small adsorbents, Ru catalysts are often used for the oxidation of various organic oxygen-containing compounds (glycerol [40], acetic acid[41], etc.). Consequently, the rise in the adsorption energy of the catalyst for the intermediate product *OOH following the addition of Ru during the OER process presents a potential issue. Namely, does the adsorption energy of intermediate products during HMFOR also experience an increase upon the introduction of Ru? At present, the methods of synthesizing single-atoms mainly include pyrolysis, wet chemistry, electrochemical and photochemical reduction method [42]. Among these methods, the electrochemical reduction presents several advantages, including simple operation, high efficiency, easy control of reaction conditions, no need for special gas conditions and no need for precursors[43].

To comprehend the aforementioned concerns, a stable bifunctional Ru monoatomic catalyst ($Ru_{0.3}$/NiFe) was synthesized using a green and uncomplicated two-step electrodeposition technique. The introduction of Ru into the crystal structure of NiFe-LDH leads to lattice expansion and alterations in electronic structure. Furthermore, electron transfer between Ru-O-M was detected by using X-ray absorption near-edge structure (XANES) and X-ray photoelectron spectroscopy (XPS) analysis. Through the application of DFT calculations, the accumulation of electrons around Ru was further disclosed. Raman spectroscopic characterization confirmed that the reactive substance is the high valence NiOOH. Specifically, the presence of single Ru atoms improves the adsorption energy of -OH, which enhances the ability of electrocatalytically generated NiOOH to capture protons in CHOH for electron transfer, thereby facilitating the conversion of HMF to DFF. This provides valuable guidance for the design of NiFe LDH catalysts and deepens the understanding of the mechanism of HMF oxidation.

2. Experimental section

The materials prepared by electrodeposition method were all processed using CHI 660D electrochemical workstation (Shanghai Chenhua Instrument Co., China), which has a three-electrode system, using saturated calomel electrode (SCE) as reference electrode and Pt wire as counter electrode.

2.1. Catalyst preparation

2.1.1. Preparation of NiFe on nickel foam (NF)

The NiFe-LDH was prepared through a straightforward electrodeposition process. During the sample processing, a 1.5 cm × 1 cm NF was meticulously cleaned by subjecting it to ultrasonication in a 1 mol/L HCl solution for 10 min to eliminate surface oxide impurities. Subsequently, NF was subjected to ultrasonic treatment in ultrapure (UP) water and ethanol for a duration of 15 min each. An aqueous solution containing Ni $(NO_3)_2 \cdot 6\ H_2O$ (16 mmol/L), $Fe(NO_3)_3 \cdot 9\ H_2O$ (10 mmol/L) and CH_3COOK (0.1 mmol/L) was used as the deposition electrolyte. The NiFe-LDH was synthesized on the working electrode by applying a constant electrodepositing potential of −1.0 V vs. SCE electrode for a duration of 10 min. Finally, the electrode was rinsed thrice with UP water and ethanol.

2.1.2. Preparation of single-atom Ru supported on NiFe

The Ru/NiFe catalyst was synthesized via an electrochemical deposition technique using a standard three-electrode system. A solution containing 0.05 mol/L NaCl and 0.3 mmol/L $RuCl_3$ was used as the electrolyte. Single-atom Ru was deposited on NiFe by potentiostatic. Determinated the deposition potential (−0.25 V vs. SCE) by cyclic voltammetry (CV). The deposition time was carefully adjusted at −0.25 V vs. SCE in order to fabricate the most efficient Ru single atom catalyst. The deposition durations for Ru were systematically varied as follows: 10 s, 20 s, 30 s, 40 s, and 50 s. The nomenclature of the catalysts was assigned based on the ICP data (Table S1) corresponding to each deposition time, resulting in $Ru_{0.04}$/NiFe, $Ru_{0.09}$/NiFe, $Ru_{0.2}$/NiFe, $Ru_{0.3}$/NiFe, and $Ru_{0.5}$/NiFe, respectively.

2.2. Electrochemical tests

The linear sweep voltammetry (LSV) curve was recorded in a 50 mL three-electrode electrochemical cell at a scanning rate of 5 mV/s with 85% iR compensation. Electrochemical impedance spectroscopy (EIS) measurements were conducted over a frequency range spanning from 0.1 Hz to 100 kHz, using an alternating current (AC) amplitude of 5 mV. The synthesized Ru/NiFe-LDH, a piece of platinum wire, and a Hg/HgO electrode (1 mol/L KOH) were utilized as the working, counter, and reference electrodes, respectively, for the oxygen evolution reaction (OER) process. The working electrolyte employed for the OER process was a 1 mol/L KOH solution. The recorded potential was normalized with respect to the reversible hydrogen electrode (RHE) according to the following procedure: $E_{RHE} = E^{\ominus}_{(Hg/HgO)} + 0.0592 \times pH + 0.098$. The stability tests were operated through i-t measurement with 24 h.

HMFOR reacted with 1 mol/L KOH and various quantities of HMF at room temperature and pressure in an H-type electrochemical cell, including 5, 7.5, 10, 12.5 mmol/L HMF (represented as HMF_5, $HMF_{7.5}$, HMF_{10}, and $HMF_{12.5}$ respectively). For the oxidation system, a range of Ru/NiFe-LDH catalysts supported on NF were utilized as the anode, a Hg/HgO electrode was implemented as the reference electrode in the anode compartment, and a Pt wire was employed as the counter electrode in the cathode compartment. The constant current experiment was carried out in an H-type electrochemical reactor, containing 35 mL 1 mol/L and 7.5 mmol HMF in each chamber. The anode and cathode chambers were separated by a Nafion 117 membrane.

2.2.1. Calculation of ECSA

The electrochemical active surface area (ECSA) was determined by measuring CV at different scanning rates ranging from 10 to 50 mV/s at no apparent Faradaic potential range (0.2–0.3 V vs. SCE). Using the plot of the current density j ((j_a-j_c)/2) at 0.25 V vs. SCE corresponding to the

various scan rates, the double layer capacitance (Cdl) was determined from the linear slope. The ECSA was obtained by dividing Cdl by the specific capacitance of a flat standard with a real surface area of 1 cm^2. In general, the specific capacitance of a flat surface is typically within the range of 20–60 μF cm^{-2} [44].

2.2.2. Turnover frequency (TOF)

The conversion of HMF, yield of FDCA, and faradaic efficiency (FE) were determined through the application of Eqs. (1–3), respectively.

$$\text{HMF conversion}(\%) = \frac{\text{n(HMF consumed)}}{\text{n(HMF initial)}} \times 100 \tag{1}$$

$$\text{FDCA yield}(\%) = \frac{\text{n(FDCA)}}{\text{n(HMF initial)}} \times 100 \tag{2}$$

$$\text{FE}(\%) = \frac{\text{n(FDCA)}}{Q/(6 \times F)} \times 100 \tag{3}$$

The Faraday constant (96,485 C mol^{-1}) was utilized as a reference value, while the mole quantity of the reactant was determined through HPLC concentration analysis and represented by the variable 'n'.

2.3. Product quantification

The oxidation products of HMF were quantitatively and qualitatively analyzed using high-performance liquid chromatography with a UV detector. The UV detector was adjusted to a wavelength of 265 nm. The mobile phase for HPLC was a mixture of 1% NH_4HCO_2/H_2O solution and methanol in a volumetric ratio of 3:7. The electrolyte was diluted 40 times before HPLC analysis.

2.4. Structural characterizations

X-ray powder diffraction (XRD) patterns obtained using a Rigaku Miniflex-600 instrument with Cu/Kα1 radiation and 40 kV were employed for the analysis of the phase structure of the prepared samples. The microstructures were examined by means of field-emission scanning electron microscopy (FESEM), utilizing the FEI QUANTA 200 F instrument. Aberration-corrected high-angle annular dark-field scanning transmission electron microscopy (AC HAADF-STEM) imaging was performed by JEOL JEM-ARM200F TEM/STEM operated at 200 kV. The elemental analysis was carried out using Inductively Coupled Plasma Optical Emission Spectrometry (ICP-OES) on an Agilent 5110 ICP-OES instrument. The photoemission spectroscopy experiments (XPS) were conducted employing Al Kα radiation (ESCALAB 250Xi K-alpha.).

2.4.1. X-ray absorption fine structure (XAFS) measurements

The analysis of Ru K-edge was conducted using Si(333) crystal monochromators at the BL14W1 beamlines of the Shanghai Synchrotron Radiation Facility (SSRF) in Shanghai, China. Prior to the examination at the beamline, the specimens were compressed into thin disks measuring 1 cm in diameter and hermetically sealed using Kapton tape film. The XAFS spectra were acquired at ambient temperature by employing a 4-channel Silicon Drift Detector (SDD) model Bruker 5040. The XAFS spectra of the standard samples, including Ru-foil, RuCl$_3$, and RuO$_2$, were acquired using the transmission mode.

2.4.2. XAFS analysis and results

The data processing and analysis were conducted using the Athena and Artemis software applications [45]. The sample's energy calibration was performed using a standard Ru-foil as a reference, which was evaluated concurrently.

To obtain global amplitude EXAFS parameters (CN, R, σ^2 and ΔE$_0$) that describe the Extended X-ray Absorption Fine Structure (EXAFS), a nonlinear least-squares fitting method was employed to fit the EXAFS equation to the Fourier-transformed data in R-space using the Artemis software. The analysis incorporated the amplitude reduction factor (S02) obtained from the EXAFS of the Ru-foil to determine the coordination numbers (CNs) in the scattering path of the sample. The Debye-Waller factors and delta Rs are obtained based on the guessing parameters and constrained for Ru-O. The technique of Wavelet transformation (WT) is implemented utilizing the software suite devised by Funke and Chukalina. The Morlet wavelet with parameters κ = 10 and σ = 1 is selected for this analysis [46,47].

2.5. DFT calculations

The DFT calculations in this study were performed using the MaterialStudio software with the CASTEP module. The plane-wave pseudopotential within the density functional theory framework and the Perdew-Burke-Ernzerhof (PBE) exchange-correlation functional were utilized [48–50]. To improve the accuracy of the calculations involving transition metals Ni, Fe and Ru, the spin-polarized DFT+U theory was utilized, with U$_{eff}$ values of 3.80 eV [51,52], 4.30 eV [53] and 4.10 eV [54] for Ni^{2+}, Fe^{3+} and Ru^{3+}, respectively. The Broyden-Fletcher-Goldfarb-Shanno algorithm was adopted to search the potential energy surface [55]. The optimal plane-wave energy of 380 eV and a 3x3x1 k-point grid were used to sample the Brillouin zone [56]. The model was considered converged when the following three conditions were satisfied: (1) energy convergence to within 2×10^{-5} eV/atom, (2) force convergence to within 0.05 eV/Å, and (3) displacement convergence to within 2×10^{-3} Å. Transition state TS is located by the dimer method. HMF adsorption energy Eads(HMF) is defined as, $E_{ads}(\text{HMF}) = E_{total}(\text{HMF/Catalyst}) - E_{total}(\text{Catalyst}) - E_{total}(\text{HMF})$. E$_{total}$(HMF/Catalyst), E$_{total}$(surface), E$_{total}$(HMF) are the total energies of the optimized surface with adsorbed HMF, the optimized empty catalyst, and the optimized HMF molecule in the gas phase.

According to the XRD data analysis, the LDH (003) crystal plane was chosen as the preferred loading surface (Fig. S1c), and the predominant crystal plane of hydrotalcite is the (003) plane [57]. The initial surface model of the (0 0 3) plane of NiFe LDH comprises two layers of metal hydroxides, wherein CO$_3^{2-}$ anions are inserted between them. The Ni and Fe components are present in a mole ratio of 5:1 within the original NiFe LDH model, and the hydrotalcite support has an elemental composition of C2H36O42Fe3Ni15. The supercell is divided by a distance of 15 Å of vacuum in the z-axis. For the single-atom Ru-loaded NiFe-LDH (003) surface model, the Ru atoms are located on the hydrotalcite laminates and face the Fe metal atoms on the laminates. Based on the ICP results, a single Ru atom is incorporated onto the crystal cell of the 3 * 3 support. The optimized configuration of the surface model is shown in Fig. S1.

3. Results and discussion

3.1. Characterization of catalytic

The Ru/NiFe catalyst is synthesized by electrodeposition, which based on the principle that metal ions are deposited on the cathode surface under the action of DC electric field or pulsed electric field. The preparation process of Ru$_{0.3}$/NiFe was shown in Fig. 1a. Firstly, NiFe LDH arranged on nickel foam (NF) was synthesized via a straightforward electrosynthesis approach as a support. The color observed after electrodeposition of NF changed from silver to brown yellow (Fig. S1a, Supporting Information). As shown in Fig. S1b, there was uniform nano sheet morphology on NF of NiFe-LDH. X-ray diffraction (XRD) pattern of the synthesized NiFe catalyst (Fig. S1c) shows the unique diffraction peak of NiFe-LDH [58]. The results of transmission electron microscopy (TEM) and XRD validated the successful preparation of LDH (Fig. S1b-c).

The Ru species deposited onto the NiFe-LDH catalyst via secondary electrodeposition from the electrolyte. To assess the dispersion of Ru atoms on LDH, the AC HAADF-STEM micrograph was acquired. The AC HAADF-STEM micrograph unequivocally illustrates the homogeneous dispersion of individual Ru atoms on the surface of NiFe (Fig. 1b and
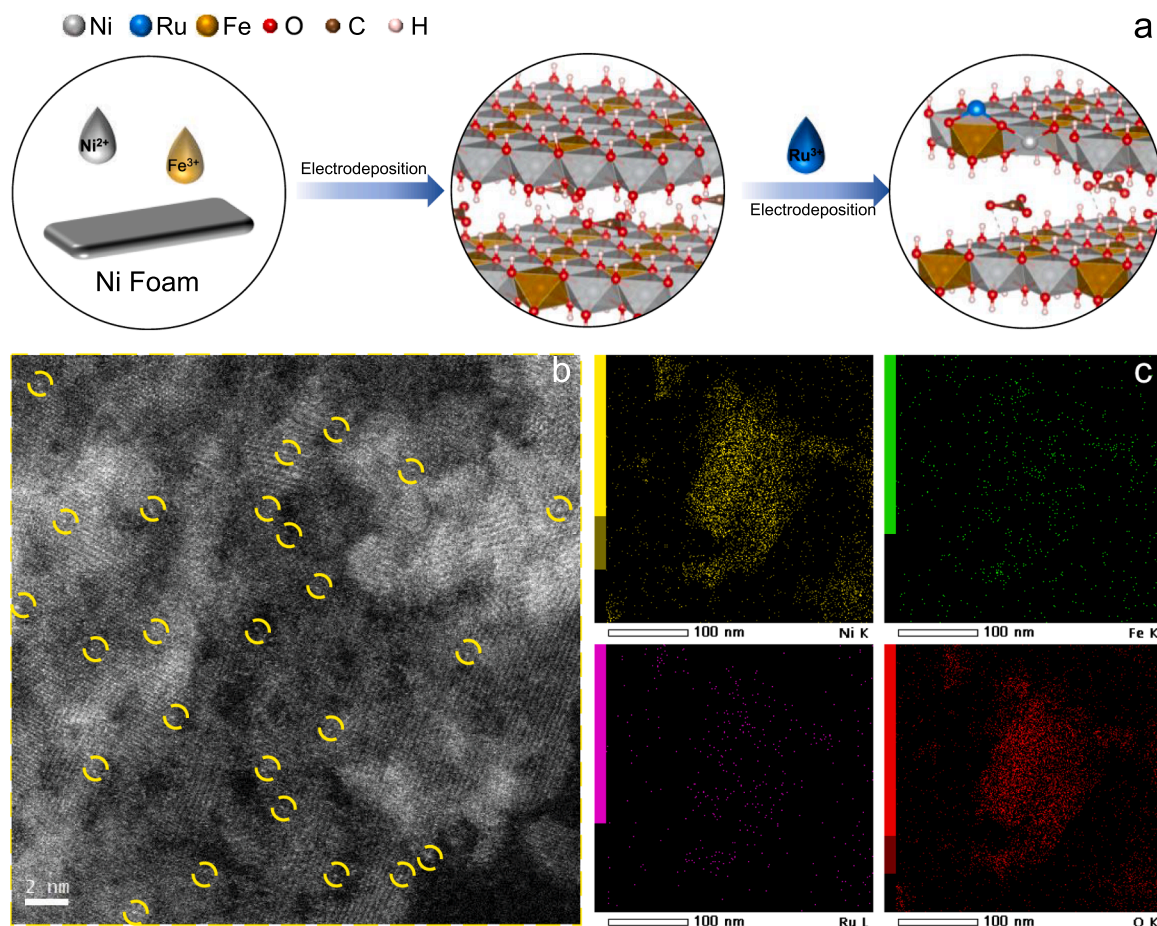
Fig. 1. a) AC HAADF-STEM image of $Ru_{0.3}$/NiFe. b) HAADF-STEM image and corresponding elemental mappings of $Ru_{0.3}$/NiFe. c) the corresponding elemental mapping images of Ni, Fe, Ru and O elements in $Ru_{0.3}$/NiFe.

Fig. S1d-e, Supporting Information). According to the illustration in Fig. S2, Ni, Fe and Ru coexisted in the synthetic catalyst. Simultaneously, energy dispersive X-ray spectroscopy (EDX) mapping results of $Ru_{0.3}$/NiFe revealed that the atomic Ru was uniformly distributed across the entire LDH (Fig. 1c). ICP-OES was applied to measure $Ru_{0.3}$/NiFe without NF. The results showed that atomic proportion of Ni to Fe was 4.9, and the Ru loading capacity was 0.3 wt%.

XPS and XANES analyses were conducted to elucidate the electronic structure of $Ru_{0.3}$/NiFe and the interaction between the single Ru atoms and the support. The peaks observed at 463.0 eV and 485.1 eV in Fig. 2a correspond to Ru $3p_{3/2}$ and Ru $3p_{1/2}$, respectively, indicating the presence of Ru in the sample with a valence state of $\delta + (0 < \delta < 3)$ [36]. Fig. 2b displays the O 1 s XPS spectra of $Ru_{0.3}$/NiFe that underwent deconvolution into three states at 529.4 (O^{2-}, named $O_{latt.}$), 531.2 (O^{2-} and O^-, named $O_{ads.}$), and 532.4 eV. The aforementioned states are in correspondence with the lattice oxygen, the oxide defects or surface oxygen ions with low coordination, and that in surface carbonate or hydroxyl species [59,60]. Note that $O_{latt.}$ peak not appears in $Ru_{0.3}$/NiFe. In addition, the binding energy of $O_{ads.}$ in $Ru_{0.3}$/NiFe has a small positive displacement of 0.2 eV, respectively, compared with that of the NiFe/LDH. This finding demonstrates that the integration of Ru ions into the surface lattice of the support can improve the concentration of oxygen vacancies. The Ru^{3+} ions, with higher electronegativity, attract electrons via the Ru-O-M bonds [35,59]. As illustrated in Fig. 3c, two obvious peaks at 852.2 and 855.8 eV, which are shown in the XPS high-resolution spectra of Ni $2p_{3/2}$ for the $Ru_{0.3}$/NiFe, are assigned to the Ni^0 and Ni^{2+}. The peaks of Ni $2p_{3/2}$ in the $Ru_{0.3}$/NiFe catalysts exhibited a positive shift of 0.3 eV in comparison with the NiFe-LDH counterpart. Concurrently, the binding energies of Fe 2p in the

$Ru_{0.3}$/NiFe showed slightly downward displacement of 0.2 eV (Fig. 2d). The valence changes of Ni and Fe may be due to the strongest ionic electronegativity of Fe^{3+}(15.38), followed by Ru^{3+}(13.52) [35]. This causes the electron cloud around Ru^{3+} to transfer to Fe^{3+}, and Ru^{3+} attracts the electron cloud of Ni^{2+}. The introduction of Ru causes a redistribution of space charge due to the synergistic electronic interactions among Ru, Ni, and Fe cations.

To figure out the valence state and coordination sphere of Ru, the XANES spectra of Ru in sample, Ru-foil, $RuCl_3$ and RuO_2 were measured. Ru K-edge XANES spectrum of Ru/NiFe has higher energy than Ru-foil but lower energy than $RuCl_3$. Linear fitting results show that the oxidation valence of Ru was 2.7 (Fig. 2e) [61]. One significant peak of Ru-O bond contribution is detected in Fourier transform (FT) k^3-weighted extended X-ray absorption fine structure (EXAFS) spectra (Fig. 2f). The deficiency of Ru–Ru and Ru–Cl coordination in the sample effaced the absence of Ru clusters and $RuCl_3$ residuals [62,63]. Furthermore, the EXAFS fitting results of the R-space spectra indicated that the coordination number of the Ru-O shell in $Ru_{0.3}$/NiFe was 3.8, suggesting the presence of the RuO_4 structure (Fig. S4; Table S2). The Ru K-edge EXAFS wavelet transforms (WT) for of Ru of the catalyst exhibited only one obvious peak at 5.3 Å^{-1}, which demonstrated that there was only one single Ru-O shell in the sample (Fig. 2g). These results suggested that the separated Ru atoms were successfully loaded on the NiFe support.

3.2. Electrocatalytic oxygen evolution reaction

To assess the electrocatalytic activity of the specimens, electrochemical measurements were carried out using a conventional three-
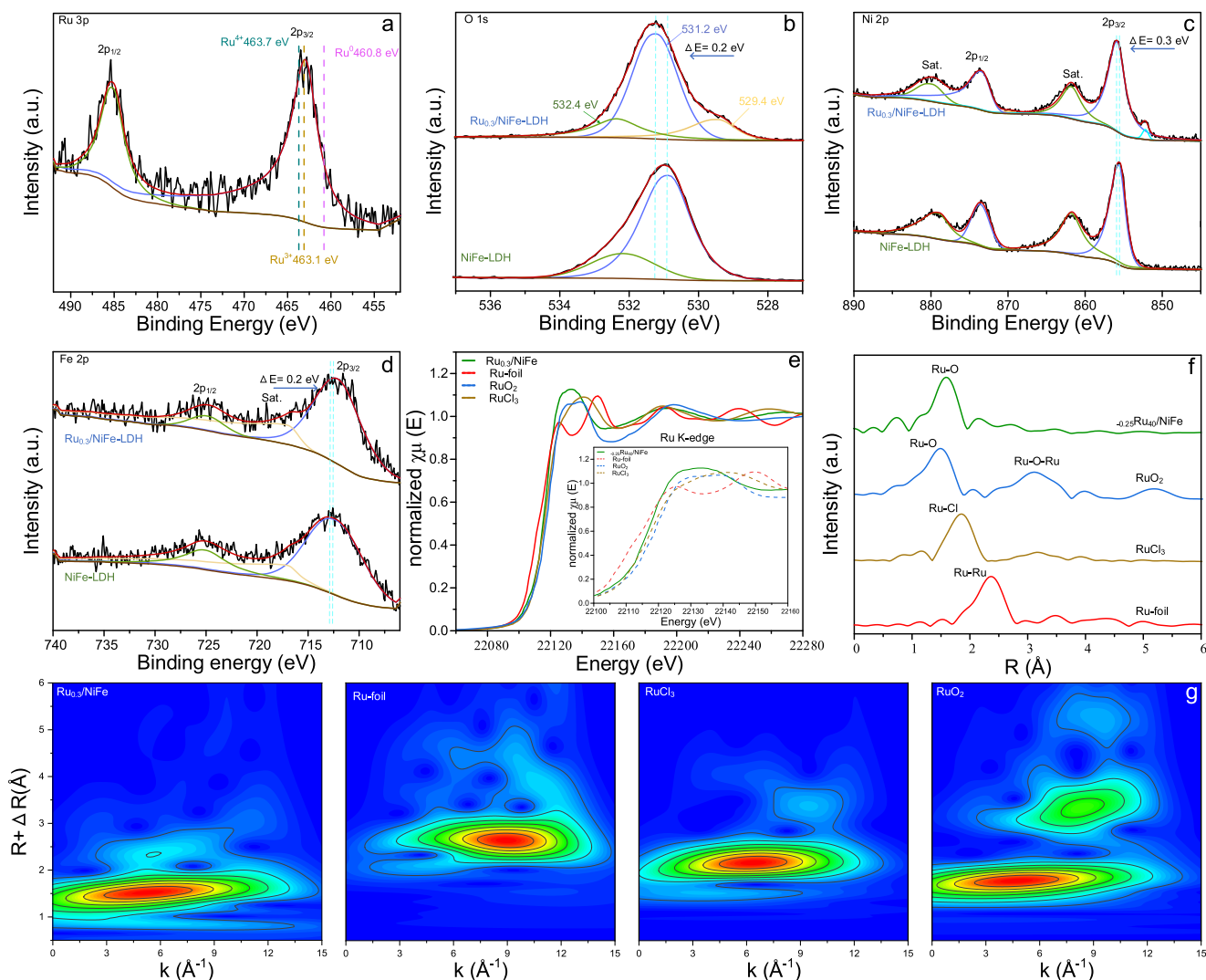
Fig. 2. XPS analysis data. a) Ru 3p XPS spectra of the Ru/NiFe-LDH. b-d) O 1 s, Fe 2p, and Ni 2p XPS spectra of the NiFe-LDH and Ru/NiFe-LDH. e) The comparison of Ru K-edge XANES spectra. f) The comparison of Ru K-edge EXAFS, shown in k2 weighted R-space. g) WT-EXAFS signals.

electrode configuration in a 1.0 mol/L KOH electrolyte. NF after electrodeposition acted as working electrode. The results obtained from linear sweep voltammetry (LSV) curves confirm that the $Ru_{0.3}$/NiFe catalyst displays the lowest onset potential compared to NF and NiFe, (Table S3). The low onset potential for $Ru_{0.3}$/NiFe was implied an enhanced *O ($M\text{-}O_{ads.}$) binding on the active interface of $Ru_{0.3}$/NiFe [60]. At a current density of 10 mA cm^{-2}, the $Ru_{0.3}$/NiFe catalyst exhibits an overpotential of 216 mV and a Tafel slope of 61 mV dec^{-1} (Fig. 3a-b). These values are markedly reduced compared to those of NF (419 mV, 111 mV dec^{-1}) and NiFe (274 mV, 86 mV dec^{-1}), as well as other Ru/NiFe samples, indicating the superior electrocatalytic performance of $Ru_{0.3}$/NiFe (Fig. 3a-b and Fig. S5a-b). The relatively lower Tafel slope and higher turnover frequency observed in $Ru_{0.3}$/NiFe imply a faster kinetic rate of the OER [23]. More importantly, $Ru_{0.3}$/NiFe also showed excellent stability in the OER process. Maintaining a current density of 12.8 mA cm^{-2} at a potential of 1.48 V_{RHE} for a period of 24 h was achieved with $Ru_{0.3}$/NiFe, as depicted in Fig. 3d. This value was found to be 4.4 and 1.3 times greater than that of NF (2.9 mA cm^{-2}) and NiFe (9.7 mA cm^{-2}), respectively.

Fig. S6 displays the CV curves used to determine the electrochemical active surface area (EASA) through the measurement of the electric double-layer capacitance (Cdl) [62]. Moreover, as illustrated in Fig. 3c, the Cdl value of $Ru_{0.3}$/NiFe was 3.98 mF cm^{-2}. This value was greater

than the Cdl values of NF (2.16 mF cm^{-2}) and NiFe (2.69 mF cm^{-2}), indicating that $Ru_{0.3}$/NiFe owned more electrochemical active sites. The increased OER activity of ECSA compared to NiFe is related to the catalyst loading of Ru. Furthermore, the electrochemical impedance spectroscopy (EIS) results demonstrate that the $Ru_{0.3}$/NiFe catalyst exhibits a lower charge transfer resistance compared to NiFe and NF (Fig. S7, Supporting Information). With an appropriate deposition time, Ru can be homogeneously deposited on NiFe (e.g., 40 s) (Fig. S8). Ru atoms will be agglomerated and unevenly distributed, when the deposition time is too long or too short.

3.3. Electrocatalytic oxidation of HMF

The catalytic performance of Ru on HMFOR was evaluated. Fig. 4a exhibits the LSV curves of HMFOR (1 mol/L KOH with 7.5 mmol/L HMF electrolyte) of $Ru_{0.3}$/NiFe, NiFe, NF in H-type cell. The overpotential of $Ru_{0.3}$/NiFe at 10 mA cm^{-2} is 64 and 213 smaller than that of NiFe and NF, respectively. Significantly, Significantly, $Ru_{0.3}$/NiFe also exhibits excellent electrochemical performance in HMFOR (Fig. S9). In comparison to OER, the catalyst exhibits a lower initial potential in HMFOR (Table S4, Supporting Information). A lower initial potential is beneficial for the progress of HMFOR. The Tafel slope of $Ru_{0.3}$/NiFe for HMFOR was merely 39 mV dec^{-1}, significantly inferior to that of NiFe
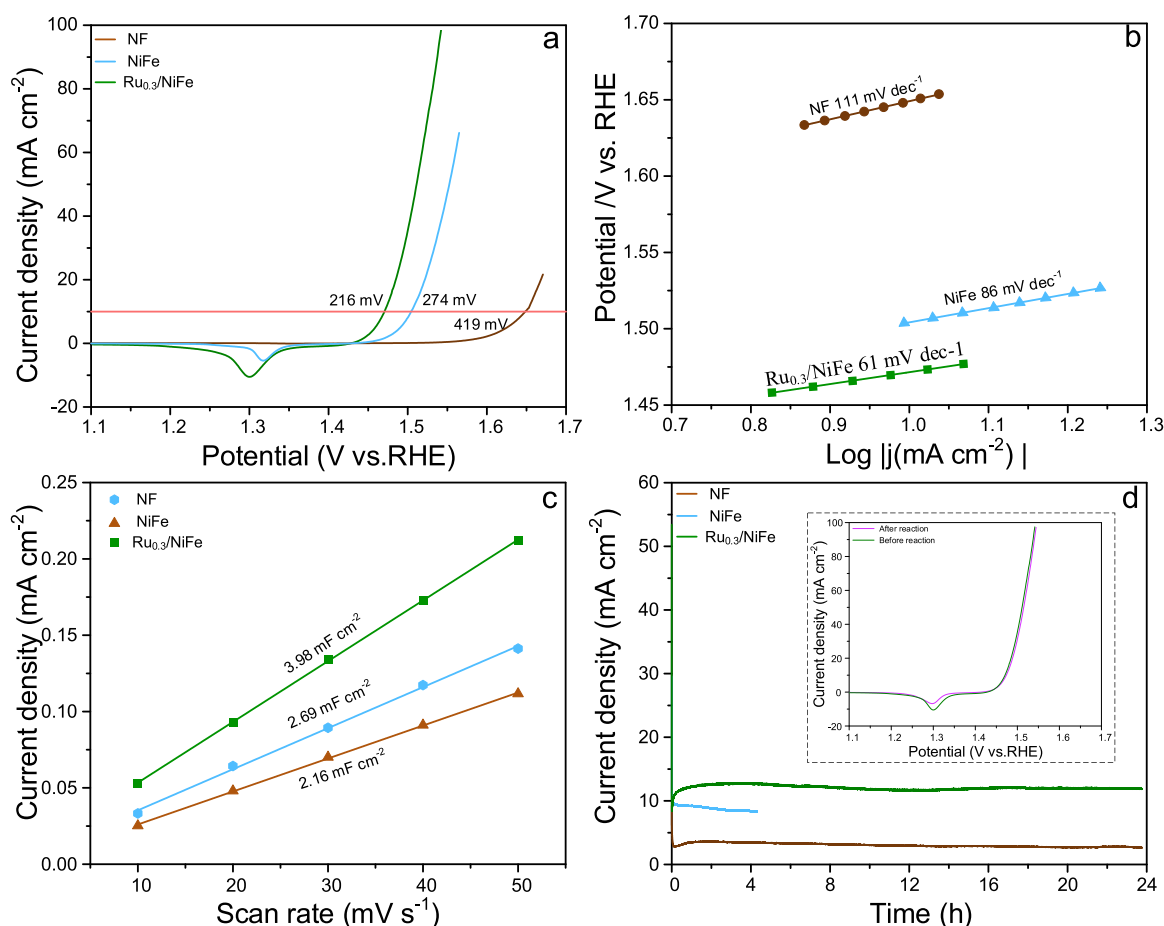
Fig. 3. Electrochemical characterization and theoretical calculations. a) LSV curves of NF, NiFe, and Ru$_{0.3}$/NiFe. b) Corresponding Tafel plots of the polarization curves in (a). c) ΔJ(Ja − Jc) of NF, NiFe and Ru$_{0.3}$/NiFe after stability test plotted against scan rates. d) chronoamperometric tests (inset shows the LSV comparison before and after the reaction).

(77 mV dec^{-1}) and NF (103 mV dec^{-1}) (Fig. 4b). EIS results show that throughout the HMFOR process, the Ru$_{0.3}$/NiFe demonstrate a lower charge transfer resistance in comparison to NiFe and NF, thereby indicating efficient electron transfer and catalytic kinetics (Fig. S10, Supporting Information). The findings suggest that the introduction of the third element, Ru, may have an effect on the electronic environment of Ni^{2+} and Fe^{3+}. Additionally, the electronically synergistic effect may contribute to the enhancement of catalytic activity [58].

Introduction of 10 mmol/L HMF into a 1 mol/L KOH electrolyte resulted in a notable negative shift in the LSV curve of Ru$_{0.3}$/NiFe (Fig. S11). Comparing the LSV curves of OER and HMFOR, the oxidation characteristics primarily arise from the oxidation of Ni(OH)$_2$ and H$_2$O in OER. The initial peak corresponds to Ni(OH)$_2$ converting to NiOOH, followed by water oxidation. In HMFOR, NiOOH acts as a chemical oxidant, facilitating HMF oxidation while being reduced to Ni(OH)$_2$ by HMF in the absence of current. Consequently, the electrochemical regeneration of NiOOH during LSV immediately participates in HMF oxidation, leading to the prompt conversion of HMF back to Ni(OH)$_2$. Thus, the presence of HMF in the solution enhances the charge transfer and facilitates the conversion of Ni(OH)$_2$ to NiOOH. In general, the presence of aldehyde and hydroxyl groups in HMF leads to two possible pathways of HMF oxidation to FDCA (Fig. 4c). In path 1, HMFCA is an intermediate product. The hydrogen atom on the aldehyde functional group of HMF is bound to the dehydrogenation site. After H on α-C is removed, OH$^-$ in the solution is absorbed, and carboxyl functional groups are formed. The path 2 involves the combination of the H on the hydroxyl functional group of HMF with the dehydrogenation site, which ultimately leads to the formation of the aldehyde group. These two

pathways form 2-formyl-5-furandicarboxylic acid (FFCA) before FDCA, and finally form FDCA. The concentrations of reactants and products were quantitatively determined by High-Performance Liquid Chromatography (HPLC). The conversion of 7.5 mmol/L HMF at different reaction times was determined at room temperature (Fig. 4d). The impact of various catalysts on the concentrations of reactants and products in HMFOR was compared. The experiments demonstrated that the HMF transformation exceeded 96% in the presence of Ru$_{0.3}$/NiFe at room temperature. To enhance the yield of FDCA, we proceeded to further optimize the reaction conditions of HMFOR (Fig. 4d, Fig. S9 and Table S4). When using 5 mmol/L HMF (Fig. 4e), the transformation of HMF was 99.2% and FDCA selectivity was 98.7%. After reaction for 4 h, the HMF conversion and FDCA yield was close to 100% and FE is about 85% at 1 h (Fig. 4f). Furthermore, Ru$_{0.3}$/NiFe exhibited superior performance compared to the majority of the documented catalysts for HMF oxidation (Table S5, Supporting Information), indicating the potential application of the Ru$_{0.3}$/NiFe electrode for practical HMF oxidation. Based on ICP analysis, the catalyst exhibited a Ru loss of 0.23% after a 4 h reaction. Furthermore, the economic profit achieved from the reaction reached an impressive 174.69%. The result demonstrated that the HMF conversion and FDCA yield increased significantly with time. Fig. 4g demonstrates the chromatograms of reactants and products at various points in time. The peak intensity of HMF (9.47 min) continued to decrease, while the peak signal of FDCA (4.17 min) gradually increased as the reaction progressed. In addition, FFCA (5.64 min) was also detected, beside of the intermediate DFF (11.11 min) and HMFCA (5.05 min). This indicates that both pathways are present in the HMF process catalyzed by Ru$_{0.3}$/NiFe.
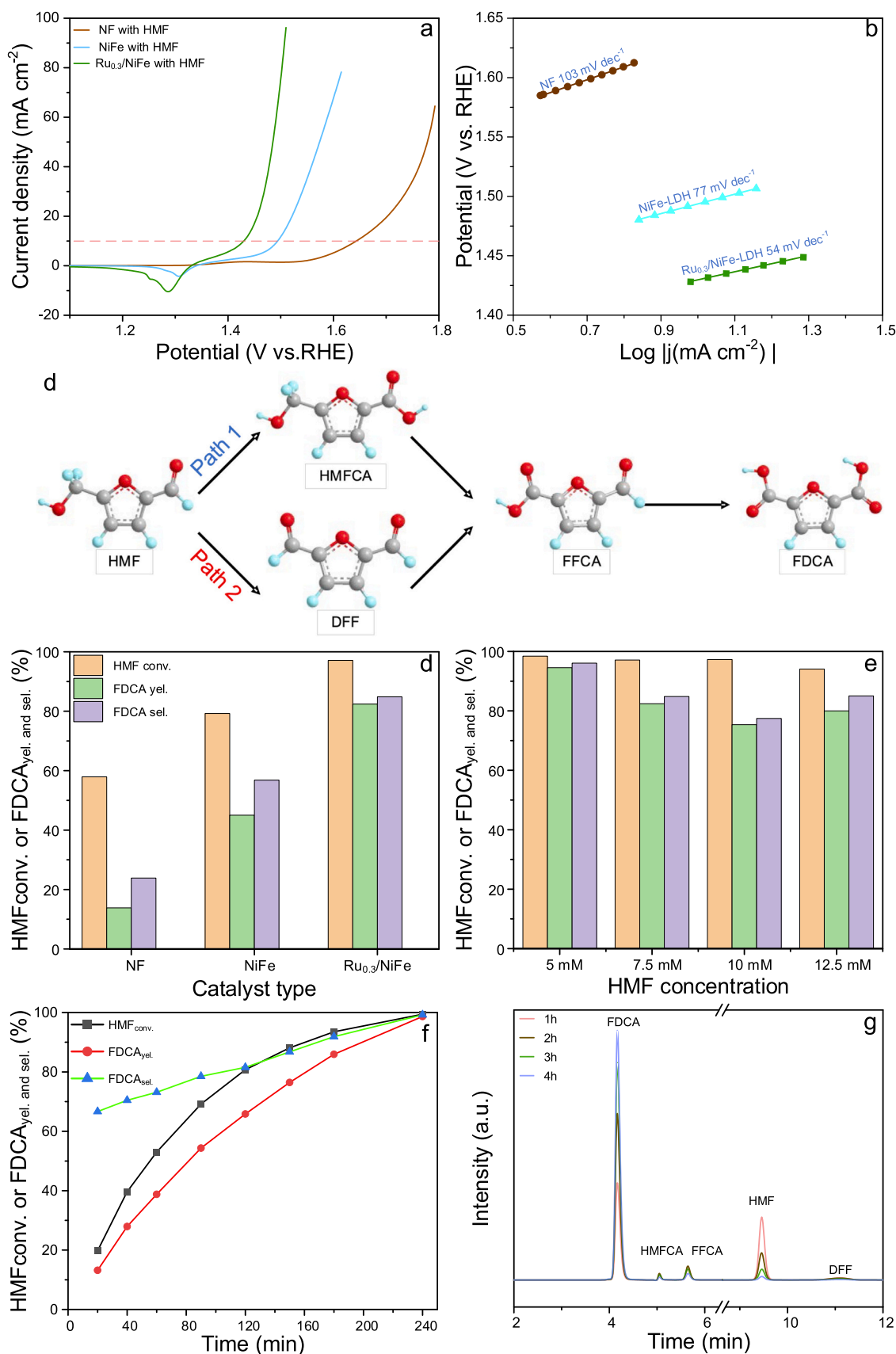
Fig. 4. a) LSV curves of electrocatalysts in 1 mol/L KOH with adding 7.5 mmol/L HMF. b) the corresponding Tafel plots. c) Schematic illustration of the two possible HMF oxidation pathways to FDCA. d) The effects of different catalysts on HMF conversion, FDCA selectivity and FDCA yield. e) Diagram of HMF conversion, FDCA selectivity and FDCA yield versus substrate concentration during the electrochemical oxidation of HMF on Ru$_{0.3}$/NiFe. f) Diagram of HMF conversion, FDCA selectivity and FDCA yield versus time during the electrochemical oxidation of HMF on Ru$_{0.3}$/NiFe (g) HPLC chromatogram during the process in f).

Reaction description: a) 7.5 mM HMF electrolyte was tested as the original solution at room temperature. b) $Ru_{0.3}$/NiFe was the catalyst at room temperature; c-d) 5 mM HMF electrolyte was tested as the original solution at room temperature. Where $HMF_{Conv.}$, $FDCA_{yel.}$ and $FDCA_{sel.}$ represent HMF conversion, FDCA yeild and FDCA selectivity respectively.

3.4. The reaction mechanism and DFT calculations

To examine the electrooxidation process of HMF on $Ru_{0.3}$/NiFe during electrolysis, the high-performance liquid chromatography (HPLC) chromatograms of intermediates and products in HMF oxidation reactions catalyzed by three catalysts (NF, NiFe, and Ru/NF) were compared at various time (Fig. S12). The contents of three intermediates in HMFOR catalyzed by NiFe were obviously higher than NF. Compared

with NF, the content of DFF in Ru/NF increased significantly during HMFOR process, indicating that the main conversion path of HMF on Ru/NF was path 2, and HMF was preferentially oxidized at the hydroxyl group. The concentration of DFF in $Ru_{0.3}$/NiFe catalyzed HMFOR process increases, while the concentration of FFCA decreases, as opposed to NiFe. The phenomenon implies that the introduction of Ru can not only promotes the oxidation of HMF hydroxyl group, but also promotes the oxidation of FFCA aldehyde group.

HMF of unabsorbed Ru species is directly catalytic oxidized by supporter (NiFe), among which deprotonated negatively charged NiO-O- surface species (superoxo species) are the catalytic active sites of HMF oxidation reaction [64,65]. Previous research has convincingly demonstrated the pronounced electrooxidation capability of high-valence nickel species towards alcohol formaldehyde biomass [66, 67]. High-valence metal (oxygen) hydroxides (NiOOH) generated
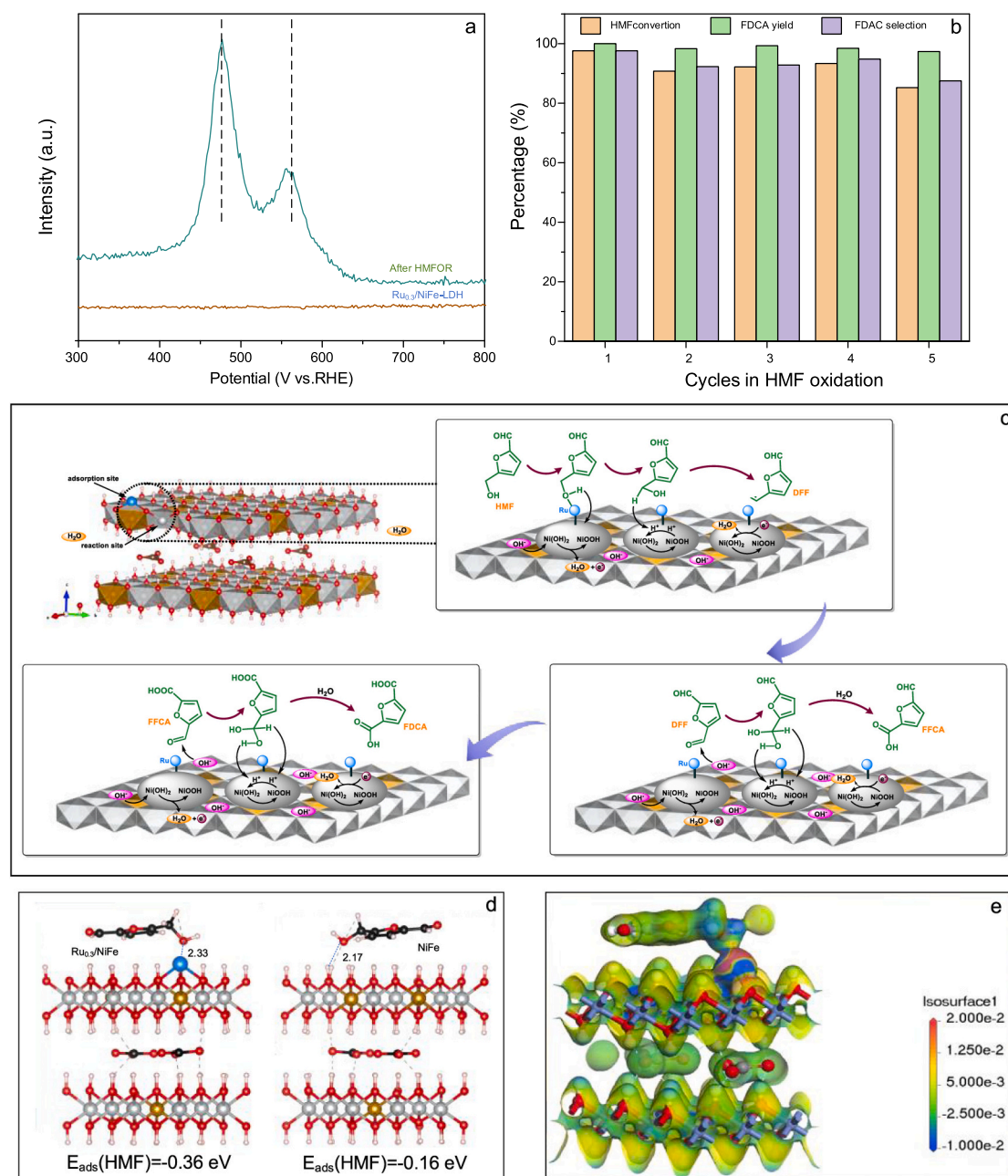
Fig. 5. a) Raman spectra of $Ru_{0.3}$/NiFe before and after HMFOR. b) HMF selectivity, FDCA conversion and selectivity obtained by $Ru_{0.3}$/NiFe for five consecutive cycles in HMF oxidation. c) $Ru_{0.3}$/NiFe catalytic process of catalytic HMF. d) Side view of HMF adsorption configuration and corresponding adsorption energy in both models. e) Charge density difference diagrams of HMF+ $Ru_{0.3}$/NiFe.

during electrochemical processes can spontaneously oxidize organic molecules without the need for an applied voltage (Fig. S13, supporting information). Once NiOOH is formed at a specific voltage, the HMFOR process will subsequently occur spontaneously [68]. To substantiate the assertion of active sites, a comparison was made between the Raman spectra of the catalysts prior to and subsequent to the reaction (Fig. 5a). As a result of the reaction, a fresh peak emerged after a duration of 4 h. The appearance of new peaks at 476 and 560 cm^{-1} within the characteristic band of NiOOH suggests that LDHs have been transformed into hydroxyl oxides during the reaction [23]. The loading of single Ru atoms is beneficial to the adsorption of HMF. The incompletely occupied e_g orbitals of Fe^{3+} and Ni^{2+} lead to weak bonding with the adsorbed oxygen species, while the vacant e_g orbitals of $Ru^{\delta+}$ may possess a stronger bonding affinity with the adsorbed oxygen species. Nonetheless, the optimum adsorption energy for oxygen species on the Ru site is achieved through partial transfer of electrons from Ni^{2+} to $Ru^{\delta+}$. In line with the Sabatier principle, the moderate binding transition metal interaction strength and adsorbed oxygen species is conducive to the HMFOR. Therefore, adjusted electronic arrangement of Ru facilitates the rapid release of DFF from the surface of $Ru_{0.3}$/NiFe catalyst. Density functional theory (DFT) computations disclosed that the Ru location on $Ru_{0.3}$/NiFe veritably provides the greatest HMFOR activity. Furthermore, electron transfer between Ni, Ru, and O sites leads to unsaturated Ru–O bonds. Meanwhile, the $Ru_{0.3}$/NiFe electrode also showed considerable durability for HMF oxidation. The HMF selectivity, FDCA conversion and selectivity still higher than 85% after five cycle reactions (Fig. 5b). No obvious fluctuation was detected during 24 h reaction, which suggested that $Ru_{0.3}$/NiFe have superior durability not only in OER, but also in HMFOR. The SEM images revealed no significant alterations in the morphology, indicating the structural integrity of the catalyst. The SEM results unanimously confirm that the single-atom catalyst can maintain stability during the electrocatalytic HMFOR process (Fig. S14, supporting information). Three intermediates were detected during the electrooxidation of HMF catalyzed by NiFe, which proved that both reaction pathways were involved in the HMFOR (Fig. 4g, and Fig. S11). This result is consistent with the previous literature [4,7].

The -OH moiety in HMF is captured by the Ru species to generate a metal alkoxide intermediate and adsorb hydrogen through cleavage of the O-H bond (Fig. 5c) [63]. Subsequently, the metal-alkoxide intermediate undergoes further transformation through β-hydrogen elimination to produce an aldehyde, thereby yielding the formation of DFF. Firstly, the Ni^{2+} is first electrochemically oxidized to Ni^{3+} ($Ni(OH)_2$ +$OH^- + e^- \rightarrow NiOOH$) during this process. The H^+ separated from HMF combine with NiOOH, and NiOOH is converted to $Ni(OH)_2$ ($C_5H_3O_2CH_2OH_{ads} + 2NiOOH + 2e^- \rightarrow C_5H_3O_2CHO_{ads}$ $Ni(OH)_2$) [3]. Then, the nucleophilic addition of OH ion and C=O bond in the solution produce hemiacetal ordiol intermediates. These intermediates are further converted into -COOH groups via dehydrogenation, forming FFCA under the action of the adsorption site Ru and the active site Ni. Finally, the OH^- ions on the surface of the catalyst react with the -CHO group to produce a hemiacetal or diol intermediate, and then the hemiacetal or diol intermediate dehydrogenates to form a COOH group [69].

The aforementioned experimental results demonstrate that under the anodic potential of HMFOR, Ru/NiFe-LDH undergoes a kinetic transition from $Ni(OH)_2$ to NiOOH. Thus, NiOOH serves as the catalytic center for HMFOR and OER. Theoretical calculations indicate that compared to OH- (Eads=−0.17 eV) and H_2O (Eads=−0.33 V), NiOOH exhibits a higher negative adsorption energy (Eads=−0.65 eV) towards HMF molecules, suggesting a stronger interaction between NiOOH and HMF. Therefore, in base electrolytes containing HMF, in-situ formed NiOOH preferentially adsorbs HMF molecules. Since the formed NiOOH is rapidly reduced by HMF, OER does not occur if the reaction between HMF and NiOOH is sufficiently fast. This calculation result aligns well with the polarization curves of different HMF concentrations with or without stirring (Fig. S17a-b). In the absence of stirring, the LSV curves in 1 M KOH with and without HMF overlap in the high potential range (Fig. S17a), indicating a deficiency of local HMF and the dominance of OER. This suggests that if the overpotential is sufficiently high or the amount of HMF on the local surface is insufficient, the unreacted portion of NiOOH is expected to be oxidized into higher-valence nickel oxides ($NiO(OH)_2$), causing OER or even OER to dominate (Fig. S17c). By further increasing the concentration of HMF in the electrolyte, the overlapping point of the two curves shifts positively (Fig. S17a). Higher HMF concentrations in the solution provide more HMF on the local surface, inhibiting OER. With increased stirring for enhanced mass transfer, the overlapping point of HMFOR also experiences a positive shift (Fig. S17b). Additionally, stirring has no impact on the LSV curve of OER.

To further examine the effect of the loading of single Ru atoms on the catalytic activity of NiFe LDH in HMFOR, spin-polarized DFT calculations were conducted, utilizing the aforementioned structure and HMF electrochemical analysis. The optimized configuration of $Ru_{0.3}$/NiFe and NiFe-LDH (003) surface models are illustrated in Fig. S15. As shown in Fig. S16, the charge density difference analysis predicts the change in charge transfer between Ru and O after loading Ru ions. A conspicuous accumulation and depletion of electrons were observed on Ru and O atoms, respectively. The result indicated the electrons transferred from O to Ru after loading Ru, in contrast to the unmodified NiFe LDH. Concurrently, multiple instances of electron depletion were detected in proximity to the Ni atom, indicative of an elevated oxidation state of Ni resulting from Ru loading, in alignment with XPS findings. Moreover, an incomplete electron transfer from Ni^{2+} to Ru^{3+} through the O bridge has been observed, which corroborated the aforementioned discourse. The high valency of Ru in comparison to Ni^{2+} results in a low coordination state of Ru atoms in NiFe-LDH, thereby creating a favorable site for HMF adsorption in the vacant orbit at the Ru site. The adsorption of HMF on the catalyst surface is a crucial step in the HMFOR process, as it is essential for its spontaneous reaction with the active species NiOOH. As shown in the simulation results in Fig. 5d-e and Fig. S18, Ru can improve the adsorption capacity of HMF. This further signified that monovalent Ru could potentially serve as the genuine adsorption nucleus, which was consistent to the experimental data. We also investigated the dehydrogenation kinetics of Ni. In addition, we also performed DFT calculations to determine the binding energies of different dehydrogenation sites (Fig. S19). The computational results revealed that Ru/FeNiOOH(4) had the lowest binding energy for H, indicating that the formation of Ru/FeNiOOH was most favorable. As shown in Table S6, under the coordination conditions of Ru/NiFe, the dehydrogenation free energy for Ni was 2.69 eV, while for NiFe it was 3.68 eV. This result indicates that the introduction of Ru facilitates the dehydrogenation of Ni, promoting the transformation from $Ni(OH)_2$ to the active catalytic phase, NiOOH. As a crucial step in HMFOR, the adsorption of HMF on the catalyst surface plays a vital role in its spontaneous reaction with the intermediate NiOOH.

4. Conclusion

In conclusion, we present a straightforward electrodeposition cationic deposition strategy for the fabrication of a dual-functional NiFe-LDH supported single Ru atoms catalyst. The $Ru_{0.3}$/NiFe catalyst exhibited outstanding catalytic performance in OER and HMFOR. Ru was successfully loaded into the NiFe-LDH structure, which was observed through a series of characterization. The electron cloud around Ru^{3+} was transferred to Fe^{3+}, and Ru^{3+} attracted the electron cloud of Ni^{2+}. The single Ru atoms loading optimizes the adsorption energy of the catalyst to HMF through electronic structure adjustments. NiOOH, an advanced Ni^{2+} species, functions as the active species during HMF reactions. Interestingly, the presence of Ru in HMFOR facilitated the formation of DFF, thereby enhancing the yield of FDCA in comparison to NiFe. Additionally, the DFT calculation results demonstrated a clear

correlation between the improvement of HMFOR activity induced by Ru loading and the modification of electronic structure. As a result of the low coordination state induced by charge transfer of Ru atoms on the crystal surface, Ru atoms become the optimal sites for the adsorption of -OH, which promotes the capture of protons from COHO in HMF by FeNiOOH generated by electrocatalysis, thereby realizing electron transfer. This study not only introduces novel concepts for dual-functional and high-performance monoatomic electrocatalysts, but also provides a profound and comprehensive mechanism for the electrocatalytic oxidation of HMF to achieve sustainable and valuable biomass production.

CRediT authorship contribution statement

Credit statements should be provided during the submission process and will appear above the acknowledgement section of the published paper as shown further below. **Haocheng Xu:** Conceptualization, Methodology, Formal analysis, Investigation, Data curation, Visualization, Resources, Writing – review & editing. **Guorong Xin:** Validation, Writing – review & editing, Supervision. **Wenxuan Hu:** Formal analysis, Visualization, Resources. **Zhengxiong Zhang:** Formal analysis, Visualization. **Chuanling Si:** Project administration. **Jingguang Chen:** Project administration. **Lefu Lu:** Resources. **Yutao Peng:** Project administration. **Xiaoyun Li:** Writing – review & editing, Project administration, Supervision, Funding acquisition.

Declaration of Competing Interest

The authors declare that they have no known competing financial interests or personal relationships that could have appeared to influence the work reported in this paper.

Data Availability

The data that has been used is confidential.

Acknowledgement

Appendix A. Supporting information

Supplementary data associated with this article can be found in the online version at doi:10.1016/j.apcatb.2023.123157.

References

[1] H. Xu, X. Li, W. Hu, L. Lu, J. Chen, Y. Zhu, H. Zhou, H. Zhou, C. Si, Recent advances on solid acid catalytic systems for production of 5-Hydroxymethylfurfural from biomass derivatives, Fuel Process. Technol. 234 (2022), 107338, https://doi.org/10.1016/j.fuproc.2022.107338.

[2] A.H. Motagamwala, K. Huang, C.T. Maravelias, J.A. Dumesic, Solvent system for effective near-term production of hydroxymethylfurfural (HMF) with potential for long-term process improvement, Energy Environ. Sci. 12 (2019) 2212–2222, https://doi.org/10.1039/C9EE00447E.

[3] H. Xu, X. Li, W. Hu, Z. Yu, H. Zhou, Y. Zhu, L. Lu, C. Si, Research Progress of highly efficient noble metal catalysts for the oxidation of 5-hydroxymethylfurfural, ChemSusChem 15 (2022), e202200352, https://doi.org/10.1002/cssc.202200352.

[4] Y. Qi, K. Wang, Y. Sun, J. Wang, C. Wang, Engineering the electronic structure of NiFe layered double hydroxide nanosheet array by implanting cationic vacancies for efficient electrochemical conversion of 5-hydroxymethylfurfural to 2,5-furandicarboxylic acid, ACS Sustain. Chem. Eng. 10 (2022) 645–654, https://doi.org/10.1021/acssuschemeng.1c07482.

[5] C. Xu, E. Paone, D. Rodríguez-Padrón, R. Luque, F. Mauriello, Recent catalytic routes for the preparation and the upgrading of biomass derived furfural and 5-hydroxymethylfurfural, Chem. Soc. Rev. 49 (2020) 4273–4306, https://doi.org/10.1039/D0CS00041H.

[6] Y. Yang, T. Mu, Electrochemical oxidation of biomass derived 5-hydroxymethylfurfural (HMF): pathway, mechanism, catalysts and coupling reactions, Green. Chem. 23 (2021) 4228–4254, https://doi.org/10.1039/d1gc00914a.

[7] W. Liu, L. Dang, Z. Xu, H.Q. Yu, S. Jin, G.W. Huber, Electrochemical oxidation of 5-hydroxymethylfurfural with NiFe layered double hydroxide (LDH) nanosheet catalysts, ACS Catal. 9 (2018).

[8] N. Zhang, Y. Zou, L. Tao, W. Chen, L. Zhou, Z. Liu, B. Zhou, G. Huang, H. Lin, S. Wang, Electrochemical oxidation of 5-hydroxymethylfurfural on nickel nitride/carbon nanosheets: reaction pathway determined by in situ sum frequency generation vibrational spectroscopy, Angew. Chem., Int. Ed. 58 (2019) 15895–15903, https://doi.org/10.1002/anie.201908722.

[9] X. Han, H. Sheng, C. Yu, T.W. Walker, G.W. Huber, J. Qiu, S. Jin, Electrocatalytic oxidation of glycerol to formic acid by CuCo₂O₄ spinel oxide nanostructure catalysts, ACS Catal. 10 (2020) 6741–6752, https://doi.org/10.1021/acscatal.0c01498.

[10] X. Zhao, X. Zhang, Z. Xue, W. Chen, Z. Zhou, T. Mu, Fe nanodot-decorated MoS₂ nanosheets on carbon cloth: an efficient and flexible electrode for ambient ammonia synthesis, J. Mater. Chem. A. 7 (2019) 27417–27422, https://doi.org/10.1039/C9TA09264A.

[11] X. Zhao, Z. Xue, W. Chen, Y. Wang, T. Mu, Eutectic synthesis of high-entropy metal phosphides for electrocatalytic water splitting, ChemSusChem 13 (2020) 2038–2042, https://doi.org/10.1002/cssc.202000173.

[12] C. Kuai, Y. Zhang, D. Wu, D. Sokaras, L. Mu, S. Spence, D. Nordlund, F. Lin, X. Du, Fully oxidized Ni-Fe layered double hydroxide with 100% exposed active sites for catalyzing oxygen evolution reaction, ACS Catal. 9 (2019) 6027–6032, https://doi.org/10.1021/acscatal.9b01935.

[13] D. Gao, F. Han, G.I.N. Waterhouse, Y. Li, L. Zhang, NiFe layered double hydroxide-derived catalysts with remarkable selectivity for the oxidation of 5-hydroxymethylfurfural to 2,5-furanedicarboxylic acid under base-free conditions, ACS Sustain. Chem. Eng. 11 (2023) 1557–1568, https://doi.org/10.1021/acssuschemeng.2c06441.

[14] Synergistic effect of multiple vacancies to induce lattice oxygen redox in NiFe-layered double hydroxide OER catalysts, Appl. Catal. B 323 (2023) 122091. https://doi.org/10.1016/j.apcatb.2022.122091.

[15] D. Friebel, M.W. Louie, M. Bajdich, K.E. Sanwald, Y. Cai, A.M. Wise, M. Cheng, D. Sokaras, T. Weng, R. Alonso-Mori, R.C. Davis, J.R. Bargar, J.K. Nørskov, A. Nilsson, A.T. Bell, Identification of highly active Fe sites in (Ni,Fe)OOH for electrocatalytic water splitting, J. Am. Chem. Soc. 137 (2015) 1305–1313, https://doi.org/10.1021/ja511559d.

[16] Z. Lu, W. Xu, W. Zhu, Q. Yang, X. Lei, J. Liu, Y. Li, X. Sun, X. Duan, Three-dimensional NiFe layered double hydroxide film for high-efficiency oxygen evolution reaction, Chem. Commun. 50 (2014) 6479–6482, https://doi.org/10.1039/C4CC01625D.

[17] W. Jiang, A.Y. Faid, B.F. Gomes, I. Galkina, L. Xia, C.M.S. Lobo, M. Desmau, P. Borowski, H. Hartmann, A. Maljusch, A. Besmehn, C. Roth, S. Sunde, W. Lehnert, M. Shviro, Composition-dependent morphology, structure, and catalytic performance of nickel–iron layered double hydroxide as highly-efficient and stable anode catalyst in anion exchange membrane water electrolysis, Adv. Funct. Mater. 32 (2022), 2203520, https://doi.org/10.1002/adfm.202203520.

[18] S. Zou, M.S. Burke, M.G. Kast, J. Fan, N. Danilovic, S.W. Boettcher, Fe (oxy) hydroxide oxygen evolution reaction electrocatalysis: intrinsic activity and the roles of electrical conductivity, substrate, and dissolution, Chem. Mater. 27 (2015) 8011–8020, https://doi.org/10.1021/acs.chemmater.5b03404.

[19] M. Görlin, P. Chernev, J. Ferreira de Araújo, T. Reier, S. Dresp, B. Paul, R. Krähnert, H. Dau, P. Strasser, Oxygen evolution reaction dynamics, faradaic charge efficiency, and the active metal redox states of Ni–Fe oxide water splitting electrocatalysts, J. Am. Chem. Soc. 138 (2016) 5603–5614, https://doi.org/10.1021/jacs.6b00332.

[20] N. Li, D.K. Bediako, R.G. Hadt, D. Hayes, T.J. Kempa, F. von Cube, D.C. Bell, L. X. Chen, D.G. Nocera, Influence of iron doping on tetravalent nickel content in catalytic oxygen evolving films, Proc. Natl. Acad. Sci. U. S. A. 114 (2017) 1486–1491, https://doi.org/10.1073/pnas.1620787114.

[21] D.K. Bediako, B. Lassalle-Kaiser, Y. Surendranath, J. Yano, V.K. Yachandra, D. G. Nocera, Structure–activity correlations in a nickel–borate oxygen evolution catalyst, J. Am. Chem. Soc. 134 (2012) 6801–6809, https://doi.org/10.1021/ja301018q.

[22] Z. Gao, J. Liu, X. Chen, X. Zheng, J. Mao, H. Liu, T. Ma, L. Li, W. Wang, X. Du, Engineering NiO/NiFe LDH intersection to bypass scaling relationship for oxygen evolution reaction via dynamic tridimensional adsorption of intermediates, Adv. Mater. 31 (2019), 1804769, https://doi.org/10.1002/adma.201804769.

[23] J. Zhang, J. Liu, L. Xi, Y. Yu, N. Chen, S. Sun, W. Wang, K.M. Lange, B. Zhang, Single-atom Au/NiFe layered double hydroxide electrocatalyst: probing the origin of activity for oxygen evolution reaction, J. Am. Chem. Soc. 140 (2018) 3876–3879, https://doi.org/10.1021/jacs.8b00752.

[24] C. Rong, X. Shen, Y. Wang, L. Thomsen, T. Zhao, Y. Li, X. Lu, R. Amal, C. Zhao, Electronic structure engineering of single-atom ru sites via Co–N4 sites for bifunctional pH-universal water splitting, Adv. Mater. 34 (2022), 2110103, https://doi.org/10.1002/adma.202110103.

[25] X. Wang, Y. Tuo, Y. Zhou, D. Wang, S. Wang, J. Zhang, Ta-doping triggered electronic structural engineering and strain effect in NiFe LDH for enhanced water

oxidation, Chem. Eng. J. 403 (2021), 126297, https://doi.org/10.1016/j.
cej.2020.126297.

[26] L. Duan, C. Hung, J. Wang, C. Wang, B. Ma, W. Zhang, Y. Ma, Z. Zhao, C. Yang,
T. Zhao, L. Peng, D. Liu, D. Zhao, W. Li, Synthesis of fully exposed single-atom-
layer metal clusters on 2D ordered mesoporous TiO₂ nanosheets, Angew. Chem.
Int. Ed. 61 (2022), e202211307, https://doi.org/10.1002/anie.202211307.

[27] M.G. Farpón, W. Henao, P.N. Plessow, E. Andrés, R. Arenal, C. Marini, G. Agostini,
F. Studt, G. Prieto, Rhodium single-atom catalyst design through oxide support
modulation for selective gas-phase ethylene hydroformylation, Angew. Chem. Int.
Ed. 62 (2022), e202214048, https://doi.org/10.1002/anie.202214048.

[28] G. Bae, S. Han, H. Oh, C.H. Choi, Operando stability of single-atom electrocatalysts,
Angew. Chem. Int. Ed. (2023), e202219227, https://doi.org/10.1002/
anie.202219227.

[29] H. Yan, M. Zhao, X. Feng, S. Zhao, X. Zhou, S. Li, M. Zha, F. Meng, X. Chen, Y. Liu,
D. Chen, N. Yan, C. Yang, PO₄³⁻ coordinated robust single-atom platinum catalyst
for selective polyol oxidation, Angew. Chem. Int. Ed. 61 (2022), e202116059,
https://doi.org/10.1002/anie.202116059.

[30] P. Rao, T. Wang, J. Li, P. Deng, Y. Shen, Y. Chen, X. Tian, Plasma induced Fe-NX
active sites to improve the oxygen reduction reaction performance, Adv. Sens.
Energy Mater. 1 (2022) 100005, https://doi.org/10.1016/j.asems.2022.100005.

[31] C. Hou, L. Zou, L. Sun, K. Zhang, Z. Liu, Y. Li, C. Li, R. Zou, J. Yu, Q. Xu, Single-
atom iron catalysts on overhang-eave carbon cages for high-performance oxygen
reduction reaction, Angew. Chem. Int. Ed. 59 (2020) 7384–7389, https://doi.org/
10.1002/anie.202002665.

[32] M. Xie, F. Dai, J. Li, X. Dang, J. Guo, W. Lv, Z. Zhang, X. Lu, Tailoring the electronic
metal–support interactions in supported atomically dispersed gold catalysts for
efficient fenton-like reaction, Angew. Chem. Int. Ed. 60 (2021) 14370–14375,
https://doi.org/10.1002/anie.202103652.

[33] Y. Yao, L. Zhao, J. Dai, J. Wang, C. Fang, G. Zhan, Q. Zheng, W. Hou, L. Zhang,
Single atom Ru monolithic electrode for efficient chlorine evolution and nitrate
reduction, Angew. Chem., Int. Ed. 61 (2022), e202208215, https://doi.org/
10.1002/anie.202208215.

[34] P. Rao, D. Wu, T. Wang, J. Li, P. Deng, Q. Chen, Y. Shen, Y. Chen, X. Tian, Single
atomic cobalt electrocatalyst for efficient oxygen reduction reaction, EScience 2
(2022) 399–404, https://doi.org/10.1016/j.esci.2022.05.004.

[35] Y. Hu, G. Luo, L. Wang, X. Liu, Y. Qu, Y. Zhou, F. Zhou, Z. Li, T. Yao, C. Xiong,
B. Yang, Z. Yu, Y. Wu, Single Ru atoms stabilized by hybrid amorphous/crystalline
FeCoNi layered double hydroxide for ultraefficient oxygen evolution, Adv. Energy
Mater. 11 (2021) 2002816, https://doi.org/10.1002/aenm.202002816.

[36] J. Su, Y. Yang, G. Xia, J. Chen, P. Jiang, Q. Chen, Ruthenium-cobalt nanoalloys
encapsulated in nitrogen-doped graphene as active electrocatalysts for producing
hydrogen in alkaline media, Nat. Commun. 8 (2017), 14969, https://doi.org/
10.1038/ncomms14969.

[37] Z. Nie, C. Zhang, X. Ding, M. Cong, F. Xu, L. Ma, M. Guo, M. Li, L. Zhang, Catalytic
kinetics regulation for enhanced electrochemical nitrogen oxidation by Ru-
nanoclusters-coupled Mn₃O₄ catalysts decorated with atomically dispersed Ru
atoms, Adv. Mater. 34 (2022), 2108180, https://doi.org/10.1002/
adma.202108180.

[38] Y. Ding, K. Cao, J. He, F. Li, H. Huang, P. Chen, Y. Chen, Nitrogen-doped graphene
aerogel-supported ruthenium nanocrystals for pH-universal hydrogen evolution
reaction, Chin. J. Catal. 43 (2022) 1535–1543, https://doi.org/10.1016/S1872-
2067(21)63977-3.

[39] Y. Sun, Z. Xue, Q. Liu, Y. Jia, Y. Li, K. Liu, Y. Lin, M. Liu, G. Li, C.-Y. Su, Modulating
electronic structure of metal-organic frameworks by introducing atomically
dispersed Ru for efficient hydrogen evolution, Nat. Commun. 12 (2021), 1369,
https://doi.org/10.1038/s41467-021-21595-5.

[40] S. Yang, Y. Chen, H. Guo, X. Jiang, J. Ma, X. Li, Z. Chen, X. Ma, Oxygen vacancies
enriched Nb-WOX supported Ru for polychlorinated aromatics oxidation: Reaction
mechanism exploration, Fuel 324 (2022), 124501, https://doi.org/10.1016/j.
fuel.2022.124501.

[41] H. Ding, X. Qi, X. Yun, J. Ge, Y. Tian, X. Lei, F. Zhang, Confined ruthenium
nanoparticles as an effective catalyst for aerobic oxidation of aqueous ethanol to
acetic acid, ACS Sustain. Chem. Eng. 10 (2022) 9687–9696, https://doi.org/
10.1021/acssuschemeng.1c08363.

[42] Y. Chen, S. Ji, C. Chen, Q. Peng, D. Wang, Y. Li, Single-atom catalysts: synthetic
strategies and electrochemical applications, Joule 2 (2018) 1242–1264, https://
doi.org/10.1016/j.joule.2018.06.019.

[43] H. Xu, Y. Zhao, G. He, H. Chen, Race on engineering noble metal single-atom
electrocatalysts for water splitting, Int. J. Hydrog. Energy 47 (2022) 14257–14279,
https://doi.org/10.1016/j.ijhydene.2022.02.152.

[44] J.D. Benck, Z. Chen, L.Y. Kuritzky, A.J. Forman, T.F. Jaramillo, Amorphous
molybdenum sulfide catalysts for electrochemical hydrogen production: insights
into the origin of their catalytic activity, ACS Catal. 2 (2012) 1916–1923, https://
doi.org/10.1021/cs300451q.

[45] B. Ravel, M. Newville, ATHENA, ARTEMIS, HEPHAESTUS: data analysis for X-ray
absorption spectroscopy using IFEFFIT, J. Synchrotron Rad. 12 (2005) 537–541,
https://doi.org/10.1107/S0909049505012719.

[46] H. Funke, A.C. Scheinost, M. Chukalina, Wavelet analysis of extended x-ray
absorption fine structure data, Phys. Rev. B. 71 (2005), 094110, https://doi.org/
10.1103/PhysRevB.71.094110.

[47] H. Funke, M. Chukalina, A.C. Scheinost, A new FEFF-based wavelet for EXAFS data
analysis, J. Synchrotron Rad. 14 (2007) 426–432, https://doi.org/10.1107/
S0909049507031901.

[48] M. Bajdich, M. García-Mota, A. Vojvodic, J.K. Nørskov, A.T. Bell, Theoretical
investigation of the activity of cobalt oxides for the electrochemical oxidation of
water, J. Am. Chem. Soc. 135 (2013) 13521–13530, https://doi.org/10.1021/
ja405997s.

[49] Y. Xu, Z. Wang, L. Tan, Y. Zhao, H. Duan, Y. Song, Fine Tuning the
Heterostructured interfaces by topological transformation of layered double
hydroxide nanosheets, Ind. Eng. Chem. Res. 57 (2018) 10411–10420, https://doi.
org/10.1021/acs.iecr.8b02246.

[50] E.B. Wilson, J.C. Decius, P.C. Cross, Molecular vibrations: The theory of infrared
and raman vibrational spectra, Cour. Corp. (1980).

[51] C. Rudolf, B. Dragoi, A. Ungureanu, A. Chirieac, S. Royer, A. Nastro, E. Dumitriu,
NiAl and CoAl materials derived from takovite-like LDHs and related structures as
efficient chemoselective hydrogenation catalysts, Catal. Sci. Technol. 4 (2014)
179–189, https://doi.org/10.1039/C3CY00611E.

[52] Y. Tokudome, T. Morimoto, N. Tarutani, P.D. Vaz, C.D. Nunes, V. Prevot, G.B.
G. Stenning, M. Takahashi, Layered double hydroxide nanoclusters: aqueous,
concentrated, stable, and catalytically active colloids toward green chemistry, ACS
Nano 10 (2016) 5550–5559, https://doi.org/10.1021/acsnano.6b02110.

[53] A. Renaud, B. Chavillon, L. Cario, L.L. Pleux, N. Szuwarski, Y. Pellegrin, E. Blart,
E. Gautron, F. Odobel, S. Jobic, Origin of the black color of NiO used as
photocathode in p-type dye-sensitized solar cells, J. Phys. Chem. C. 117 (2013)
22478–22483, https://doi.org/10.1021/jp4055457.

[54] M. Wang, Y. Thimont, L. Presmanes, X. Diao, A. Barnabé, The effect of the oxygen
ratio control of DC reactive magnetron sputtering on as-deposited non
stoichiometric NiO thin films, Appl. Surf. Sci. 419 (2017) 795–801, https://doi.
org/10.1016/j.apsusc.2017.05.095.

[55] Y. Zhao, X. Jia, G. Chen, L. Shang, G.I.N. Waterhouse, L. Wu, C. Tung, D. O`Hare,
T. Zhang, Ultrafine NiO nanosheets stabilized by TiO₂ from monolayer NiTi-LDH
precursors: an active water oxidation electrocatalyst, J. Am. Chem. Soc. 138 (2016)
6517–6524, https://doi.org/10.1021/jacs.6b01606.

[56] Y. Xu, Z. Wang, L. Tan, H. Yan, Y. Zhao, H. Duan, Y. Song, Interface engineering of
high-energy faceted Co₃O₄/ZnO heterostructured catalysts derived from layered
double hydroxide nanosheets, Ind. Eng. Chem. Res. 57 (2018) 5259–5267, https://
doi.org/10.1021/acs.iecr.8b00170.

[57] D.G. Evans, R.C.T. Slade, Structural Aspects of Layered Double Hydroxides, in:
X. Duan, D.G. Evans (Eds.), Layered double hydroxides, Springer, Berlin,
Heidelberg, 2006, pp. 1–87, https://doi.org/10.1007/430_005.

[58] M. Zhang, Y. Liu, B. Liu, Z. Chen, H. Xu, K. Yan, Trimetallic NiCoFe-layered double
hydroxides nanosheets efficient for oxygen evolution and highly selective
oxidation of biomass-derived 5-Hydroxymethylfurfural, ACS Catal. 10 (2020)
5179–5189, https://doi.org/10.1021/acscatal.0c00007.

[59] H. Huang, Q. Dai, X. Wang, Morphology effect of Ru/CeO₂ catalysts for the
catalytic combustion of chlorobenzene, Appl. Catal., B 158–159 (2014) 96–105,
https://doi.org/10.1016/j.apcatb.2014.01.062.

[60] J. Zhao, S. Xu, H. Wu, Z. You, L. Deng, X. Qiu, Metal–support interactions on Ru/
CaAlOx catalysts derived from structural reconstruction of Ca–Al layered double
hydroxides for ammonia decomposition, Chem. Commun. 55 (2019)
14410–14413, https://doi.org/10.1039/C9CC05706D.

[61] J. Chen, H. Li, C. Fan, Q. Meng, Y. Tang, X. Qiu, G. Fu, T. Ma, Dual Single-atomic
Ni-N4 and Fe-N4 sites constructing janus hollow graphene for selective oxygen
electrocatalysis, Adv. Mater. 32 (2020) 2003134, https://doi.org/10.1002/
adma.202003134.

[62] C.C.L. McCrory, S. Jung, J.C. Peters, T.F. Jaramillo, Benchmarking heterogeneous
electrocatalysts for the oxygen evolution reaction, J. Am. Chem. Soc. 135 (2013)
16977–16987, https://doi.org/10.1021/ja407115p.

[63] J. Jiang, A. Kucernak, Mesoporous microspheres composed of PtRu Alloy, Chem.
Mater. 16 (2004) 1362–1367, https://doi.org/10.1021/cm035237j.

[64] B.J. Taitt, D. Nam, K. Choi, A comparative study of nickel, cobalt, and iron
oxyhydroxide anodes for the electrochemical oxidation of 5-hydroxymethylfurfural
to 2,5-furandicarboxylic acid, ACS Catal. 9 (2019) 660–670, https://doi.org/
10.1021/acscatal.8b04003.

[65] O. Diaz-Morales, D. Ferrus-Suspedra, M.T.M. Koper, The importance of nickel
oxyhydroxide deprotonation on its activity towards electrochemical water
oxidation, Chem. Sci. 7 (2016) 2639–2645, https://doi.org/10.1039/C5SC04486C.

[66] M.T. Bender, Y.C. Lam, S. Hammes-Schiffer, K.S. Choi, Unraveling two pathways
for electrochemical alcohol and aldehyde oxidation on NiOOH, J. Am. Chem. Soc.
142 (2020) 21538–21547, https://doi.org/10.1021/jacs.0c10924.

[67] R. Luo, Y. Li, L. Xing, N. Wang, R. Zhong, Z. Qian, C. Du, G. Yin, Y. Wang, L. Du,
A dynamic Ni(OH)₂-NiOOH/NiFeP heterojunction enabling high-performance E-
upgrading of hydroxymethylfurfural, Appl. Catal., B 311 (2022) 121357, https://
doi.org/10.1016/j.apcatb.2022.121357.

[68] Y. Sun, J. Wang, Y. Qi, W. Li, C. Wang, Efficient electrooxidation of 5-hydroxy-
methylfurfural using Co-Doped Ni₃S₂ catalyst: promising for H₂ production under
industrial-level current density, Adv. Sci. 9 (2022), 2200957, https://doi.org/
10.1002/advs.202200957.

[69] X. Wan, C. Zhou, J. Chen, W. Deng, Q. Zhang, Y. Yang, Y. Wang, Base-free aerobic
oxidation of 5-hydroxymethyl-furfural to 2,5-furandicarboxylic acid in water
catalyzed by functionalized carbon nanotube-supported Au–Pd alloy nanoparticles,
ACS Catal. 4 (2014) 2175–2185, https://doi.org/10.1021/cs5003096.